

# Application of Ion Imaging to the Study of Unimolecular and Bimolecular Reactions\*

Theofanis N. Kitsopoulos  
Combustion Research Facility, Sandia National Laboratories, PO Box 969  
Livermore, CA 94550

Mark A. Buntine  
Chemistry Department, Yale University, New Haven, Conn.

David P. Baldwin  
Ames Research Laboratory, Iowa State University, Ames, Iowa, 50011

Richard N. Zare  
Chemistry Department, Stanford University, Stanford CA, 94305

and

David W. Chandler  
Combustion Research Facility, Sandia National Laboratories, PO Box 969  
Livermore, CA 94550

## Abstract

We use the photofragment ion imaging technique to investigate the 266-nm photodissociation dynamics of hydrogen iodide. We show the quantitative features of ion imaging by comparing determinations of photofragment recoil velocity distributions, product branching ratios and the HI bond dissociation energy with previously published results. Excellent agreement with previous experimental and theoretical results is obtained. The H atoms produced from this process are then used as reactants in the reaction of  $\text{H} + \text{HI}$  and  $\text{H} + \text{D}_2$ . Imaging techniques are used to measure the velocity distributions of the products of these reactions.

## 1. Introduction

Photofragment ion imaging is a relatively new experimental technique first demonstrated in 1987 by Chandler and Houston.<sup>1</sup> Since the initial report, ion imaging has been used to study the dynamics of a variety of unimolecular photodissociation processes.<sup>2-5</sup> The technique allows for a *direct* two-dimensional (2-D) visualization of laboratory-frame photofragment velocity distributions. As such, photofragment ion imaging provides a powerful multiplexing advantage over more established one-dimensional Doppler<sup>6-8</sup> and time-of-flight<sup>9,10</sup> spectroscopic techniques in elucidating complete three-dimensional center-of-mass photofragment velocity distributions. In order to demonstrate the quantitative nature of the ion imaging and to provide a sense of the power (and limitations) of direct 2-D visualization of the velocity distribution of reaction products, we apply of ion imaging to the 266-nm photodissociation of hydrogen iodide (HI). Study of this process is also important for the understanding of subsequent bimolecular reaction studies.

The gas phase photodissociation of HI using ultraviolet radiation has been widely studied, both experimentally<sup>7-17</sup> and theoretically<sup>18,19</sup> since the mid 1930's. Mulliken<sup>18</sup> predicted in 1937 that the first ultraviolet continuum of HI, a broad, featureless absorption peaking around 220 nm,<sup>20</sup> arises from one parallel- and two perpendicular-type electronic transitions.<sup>21</sup> Mulliken assigned the parallel transition as  $^3\Pi_0^+ \leftarrow ^1\Sigma^+$  and the two perpendicular transitions as  $^3\Pi_1 \leftarrow ^1\Sigma^+$  and  $^1\Pi \leftarrow ^1\Sigma^+$ . Mulliken believed that a fourth repulsive state in the first absorption continuum, the  $^3\Sigma^+$  state, was too high in energy to contribute any parallel character to the dissociation process. Here we present our study of the 266-nm photolysis of HI.

One of the ultimate goals in the field of reaction dynamics<sup>22</sup> is to be able to measure the angular distribution of products in a quantum-state-specific manner. As a step in this direction, we reported the first application of ion imaging<sup>23</sup> to a bimolecular reaction. We studied the  $\text{H} + \text{HI} \rightarrow \text{H}_2 + \text{I}$  reaction in a neat supersonic molecular beam of HI. The supersonic expansion provides a reaction precursor possessing a very narrow thermal velocity distribution. Because the HI source was not thermal equilibrated (eg. an effusive beam, or bulb), the center-of-mass collision energy spread was substantially reduced. Fast H atoms were formed by laser photolysis of HI at 266 nm, and the  $\text{H}_2$  ( $v=1$ ,  $J=11,13$ ) products are ionized by (2+1) resonance-enhanced multiphoton ionization (REMPI)<sup>24</sup> before being imaged onto a position-sensitive detector. In this way we have measured the laboratory-frame speed distribution of the state-selected reaction products. Early dynamical studies of the  $\text{H} + \text{HI}$  abstraction reaction attempted to measure the angular distribution of the molecular product but failed because of background problems<sup>25,26</sup>. More recently, internal state distributions of the molecular product have been determined, but without angular information<sup>27-29</sup>. In our study of the  $\text{H} + \text{HI}$  reaction we were able to determine the speed distribution of a particular product with a particular quantum state populated,  $\text{H}_2$  ( $v=1$ ,  $J=11,13$ ). Ideally, one would like to measure the velocity distribution, both speed and angular, of the reaction products the differential cross-section (DCS) measurement. This can only be done if the velocities of the reagents are well defined. We have produced an apparatus that allows us to both define the relative velocity of the reagents and image the entire angular distribution of the products at the same time. We call this Reaction Product Imaging, RPI.

In our laboratory, we have implemented a novel ion imaging technique for studying the differential cross section of a neutral bimolecular reaction. This experiment demonstrates the power of the technique in several ways. First, by designing the experiment such that the symmetry axis of the product velocity distribution is oriented parallel to the face of the imaging detector, one image is all that is required to define uniquely the three-dimensional angular distribution. Second, the multiplexing advantage of measuring all angles at once reduces the time necessary to determine a velocity distribution. Third, there are two modes of operation offered by the technique. One mode involves imaging of the atomic reaction product, which results in moderate energy resolution measurements comparable to conventional time-of-flight experiments. Ion images of atomic products are extremely useful in providing the overall appearance of the differential cross section for a reaction or photofragmentation process, since they contain information concerning all product channels. The alternative mode relies on imaging of the molecular fragment or reaction product in a quantum state-selective manner, thus enabling differential cross section measurements for a single rovibronic state of the molecular product. We report here our preliminary measurements of the DCS for the  $\text{H} + \text{D}_2 \rightarrow \text{HD} + \text{D}$  reaction using ion imaging of the D-atom product. The reaction is studied at relative collision energies of 0.54 and 1.29 eV.

## 2. HI Photolysis

Clear, Riley and Wilson<sup>9</sup> provided the first direct experimental evidence that both parallel- and perpendicular-type dissociation channels are active in HI dissociation. Using their time-of-flight (TOF) photofragment mass spectrometer, these workers showed that 266-nm HI dissociation occurring along the parallel transition path resulted in the formation of translationally hot ground state H atoms and electronically excited  $\text{I}^*$  ( $^2\text{P}_{1/2}$ ) atoms. Conversely, they showed that HI dissociation occurring along the perpendicular transition paths resulted in the formation of even faster ground state H atoms concomitant

with ground state I ( $^2P_{3/2}$ ) atoms. In addition, they determined that  $36\pm 5\%$  of the iodine atoms are formed in the excited electronic state.

In a subsequent study, Schmiedl *et al.*<sup>8</sup> employed laser induced fluorescence Doppler spectroscopy to probe the recoil energy, angular distribution and branching ratio of the H-atom fragment following 266-nm HI photolysis. This study produced results in good agreement with the earlier experiments, determining a yield of  $40\pm 5\%$  for excited state  $I^*$  production. In 1983, Van Veen *et al.*<sup>10</sup> undertook a series of angle-resolved TOF experiments probing H-atom distributions following HI photolysis at 248, 222 and 193 nm. Together with the data reported following 266-nm photolysis, these workers were able to generate potential energy curves for the relevant excited states involved in the dissociation process and determine the  $I^*/I$  branching ratio as a function of photolysis energy. Their results were in good agreement with those of Mulliken and Clear *et al.* with the exception that the fourth state, the  $^3\Sigma^+$  state, was found to be much lower in energy than given by Mulliken and as such has a small, yet significant, contribution to  $I^*$  production at photolysis wavelengths shorter than 248 nm. Van Veen *et al.* provided the first experimental evidence that excited state  $I^*$  production following HI photolysis at 248, 222 and 193 nm originates from a mixed transition. That is, from a transition containing both parallel and perpendicular character. This observation indicated that the dynamics of HI dissociation below 248 nm could not simply be explained by invoking an adiabatic Born-Oppenheimer formalism as had been generally assumed until this time. In future studies it would be necessary to consider nonadiabatic couplings between the repulsive potential energy surfaces in question.

A comprehensive theoretical investigation of the photodissociation dynamics of HI has been reported by Levy and Shapiro.<sup>19</sup> These workers generated nonadiabatic potential energy curves for the first four excited electronic states of HI,  $I^*/I$  product branching ratios as a function of dissociation wavelength, and anisotropy parameters describing the dissociation dynamics. This study utilized a semi-empirical parameterization of experimental data reported in the literature rather than undertaking *ab initio* calculations. They determine a yield of 39.3%  $I^*$  for the photolysis at 266 nm.

With the near ultraviolet photodissociation dynamics of HI being so well characterized, this molecule presents itself as an ideal candidate with which to quantitatively assess the performance of ion imaging. Here we report our results on the 266-nm dissociation of HI in a supersonic molecular beam. H-atom photofragments are resonantly ionized by a second UV laser beam and the  $H^+$  fragment laboratory-frame velocity distribution is probed with a position sensitive ion detector. We quantitatively demonstrate that ion imaging is a powerful technique for determining the symmetry of dissociation pathways, product branching ratios and complete 3-D fragment velocity distributions.

## 2.2 Experimental Procedure

The experimental apparatus used to perform photofragment ion imaging experiments is conceptually quite straightforward and has been reported in the literature a number of times.<sup>1-5</sup> Figure 1 shows a schematic diagram of the apparatus. A supersonic expansion of HI (Matheson, stated purity 98.0%, used without further purification) seeded in helium (seed ratio 1:5) is introduced into the vacuum chamber through a pulsed solenoid valve (Series 9, General Valve Corp.) having a 0.8 mm diameter orifice. The backing pressure behind the nozzle is maintained at 1000 Torr, while the operating pressure in the source chamber typically rises to  $5 \times 10^{-5}$  Torr when the nozzle is operating. The ensuing molecular beam is collimated by a 0.5-mm diameter skimmer (Beam Dynamics) before entering the reaction and detection region in which the operating pressure is maintained at approximately  $8 \times 10^{-8}$  Torr.

Approximately 5 cm downstream from the nozzle orifice, the skimmed molecular beam, having passed through a small hole in an ion repeller plate, is intersected by a lightly focused 266-nm laser beam whose linear polarization axis lies perpendicular to the molecular beam propagation axis. The 266 nm

radiation is generated by the frequency-quadrupling of an injection-seeded Nd:YAG laser (Quanta Ray DCR-2A; seeder Quanta Ray 6300) and serves to dissociate the HI in the molecular beam. The polarization axis of this dissociation laser defines an axis of cylindrical symmetry for the recoil velocity distribution of the HI photofragments. As will be described below, the correct laboratory-frame spatial orientation of this dissociation axis is critical to correctly performing these experiments.

A co-linear, counterpropagating, tunable ultraviolet laser beam ( $\sim 205$  nm), which is generated by doubling the output of an injection-seeded Nd:YAG-pumped dye laser (Quanta Ray DCR-3A; seeder Quanta Ray 6300; Quanta Ray PDL 2, dye R640) in a  $\text{KD}^*\text{P}$  crystal and mixing the frequency-doubled output with residual dye laser fundamental in a BBO crystal, is used to ionize the H-atom photofragments from the HI dissociation process. The H-atom ionization laser beam is focussed onto the molecular beam by an 11-inch focal length lens. Precise adjustment of the position of the ionization laser focal volume in space allows for it to be enveloped by the larger dissociation laser focal volume. This experimental geometry ensures efficient ionization of all photofragment velocity components within the laser bandwidth. The frequency of the ionization laser is scanned in order to sample the full Doppler profile of the dissociation fragments.

H-atom ionization occurs via (2+1) resonance-enhanced multiphoton ionization (REMPI) through the H ( $n=3$ ) intermediate state. The ionization laser frequency is half that of the H-atom Lyman- $\beta$  transition frequency. A delay of 10 ns between the molecular dissociation laser pulse and the photofragment H-atom ionization laser pulse is short enough to ionize recoiling photofragments within the laser bandwidth before they have a chance to escape from the ionization laser focal volume, but not so short as to initiate ionization before the dissociation process is complete. Both the dissociation and ionization laser pulses have an approximate 5 ns duration.

Photofragment  $\text{H}^+$  ions are accelerated along the molecular beam propagation axis into a conventional time-of-flight (TOF) mass spectrometer. At the end of the TOF drift region the ions impinge upon a position-sensitive detector (Galileo). This detector consists of a chevron-type microchannel plate (MCP) assembly behind which is mounted a fast phosphor screen. The front plate of the detector is normally maintained at ground potential, effectively operating the MCP below threshold voltage. In order to detect only those  $\text{H}^+$  ions of interest and reject all other photoions (such as  $\text{HI}^+$ ), the front plate of the MCP is pulsed to  $-650$  V at the appropriate arrival time.<sup>2,30</sup> During the 50 ns duration of this pulse, the MCP gain is approximately  $10^6$ - $10^7$ . Mounted behind the MCP assembly is a fast phosphor screen (Galileo,  $t_{1/2} \sim 50$  ns) maintained at 2.5 kV above the potential of the rear MCP plate, behind which is a fiber-optic bundle that couples the detector phosphorescence out of the vacuum chamber. Photofragment ion images from the phosphor screen are recorded by imaging the output of the fiber-optic bundle onto a Peltier-cooled,  $384 \times 576$  pixel array charge-coupled device (CCD) (Photometrics, CC200) with a standard 35-mm camera lens assembly. Signal averaging is performed by keeping the CCD camera shutter open over, typically, 2,000 to 5,000 laser shots.

The Doppler width of the H-atom fragments generated following 266-nm dissociation of HI exceeds the bandwidth of the ionization laser. In order to sample all photofragments equally, the frequency of the ionization laser is scanned while an image is being recorded by the CCD.<sup>2</sup> Scanning the ionization laser frequency in this manner produces an effective "top hat" frequency profile over the entire H-atom Doppler width. The integrated charge on the CCD is read once by the associated camera electronics and transferred to a personal computer for storage and manipulation. By timing the molecular beam to arrive after the laser pulses, a separate background exposure is recorded which is subtracted from the photodissociation image to remove the effects of ambient light and non-resonant background ion production.

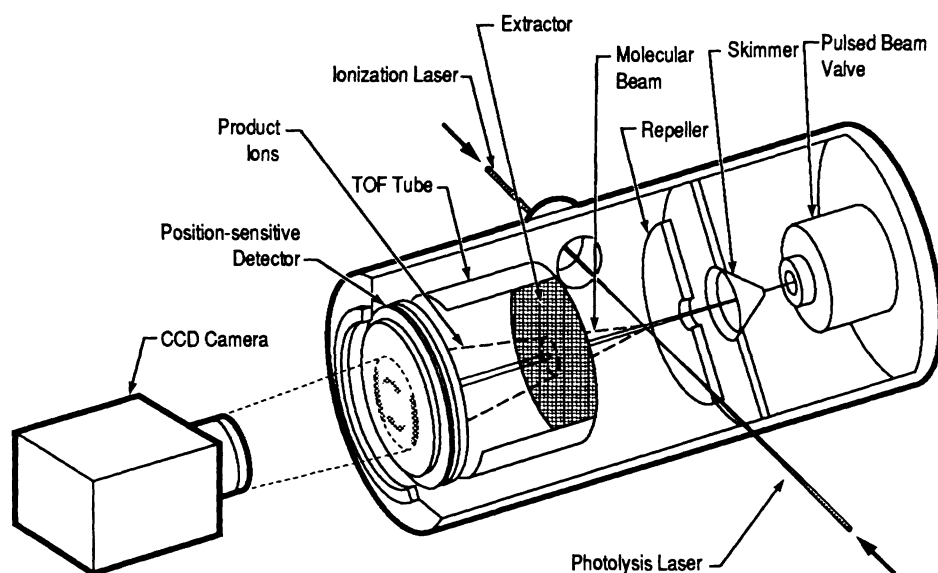


**Figure 1**

Schematic diagram of the photofragment ion imaging apparatus. Jet-cooled HI is photolyzed by a vertically polarized 266-nm dissociation laser and the H-atom fragments are resonantly ionized by a counterpropagating 205-nm laser ( $1/2 L_{\beta}$ ). The ionized fragments are projected onto an ion detector which consists of a pair of microchannel plates coupled to a phosphor screen. An ion image is recorded from the phosphor screen by a CCD camera.

Photofragment ion images represent a two-dimensional projection along an axis perpendicular to the detector plane of the three-dimensional velocity distribution of ionized photofragments. In our experimental apparatus, this projection axis is identical to the propagation direction of the molecular beam. We refer to this axis as the detector axis and always orient the linear polarization vector of the dissociation laser perpendicular to this axis (vertical polarization in the laboratory frame). Orientation of the dissociation laser polarization vector in this way defines an axis of cylindrical symmetry for the photofragment recoil velocity distribution that is perpendicular to the detector axis. When these symmetry conditions are satisfied, the 3-D velocity distribution may be reconstructed from its 2-D projection by computing the inverse Abel transform of the ion image.<sup>31</sup> The methodology for reconstructing 3-D velocity distribution of ionized photofragments has been described in detail by Strickland and Chandler.<sup>32</sup> These workers detail the mathematical algorithm used to perform the Abel inversion and discuss the experimental limitations of this technique. One important point to keep in mind is that the focussed ionization laser beam does not create a point source ionization volume. Photofragment ionization occurs throughout the molecular beam-ionization laser beam interaction region. This situation results in minor blurring of the ion images along the laser propagation axis. As described by Strickland and Chandler, this blurring can be successfully accounted for when performing an image reconstruction. No such blurring is evident along the axis perpendicular to both the laser propagation direction and the detector axis.

### 2.3 Results and Discussion

Figure 2 is an ion image of fragment H atoms ionized following the 266-nm photodissociation of HI. There are two distinct types of fragment distribution evident in this image. Remembering that this ion image is a 2-D projection of the 3-D H-atom velocity distribution, fragments are clearly seen to arise from competing parallel- and perpendicular-type dissociation pathways. The intense lobes at the top and bottom of the image correspond to photofragments arising from a parallel dissociation pathway. Conversely, ion intensity found at the sides of the image arise from perpendicular dissociative transitions. As described in the introduction, it has been previously determined that a parallel dissociation mechanism produces electronically excited iodine fragments,<sup>8-10</sup> whereas a perpendicular dissociative pathway forms ground state iodine. Accordingly, H-atom fragments produced from a parallel dissociation will have less velocity

than those formed from a perpendicular channel. The different radii of the cosine- and sine-squared fragment distributions in Fig. 2 support this observation. Analysis of Fig. 2 provides a quantitative description of HI dissociation dynamics as well as a test of the performance of the ion imaging technique compared to Doppler spectroscopy or TOF experimental methods.

As long as the arrival time at the detector is known, the speed of the fastest H atoms travelling perpendicular to the detector axis can be determined from Fig. 2. This is achieved by measuring the baseline width of an ion image intensity profile taken as a thin vertical slice down the center of the image (a horizontal intensity profile would be along the blurred axis). Such a determination directly provides a measurement of the HI bond dissociation energy from the 2-D projection. Figure 3 shows a vertical intensity profile of Fig. 2. The greatest error in determining the fragment speed arises from uncertainties in measuring the image size. Errors associated with measuring ion arrival times are insignificant. From the baseline extrapolation shown in Fig. 3 we calculate that the fastest H atoms following 266-nm HI photolysis, moving perpendicular (vertical) to the detector axis possess  $0.66 \pm 0.04$  eV of translational energy. These photofragments are formed via a parallel dissociation pathway concomitant with excited state  $^2P_{1/2}$  iodine atoms. It is known that the energy difference between  $I(^2P_{3/2})$  and  $I^*(^2P_{1/2})$  is  $0.94$  eV,<sup>33</sup> so we expect H atoms formed from a perpendicular dissociation pathway (concomitant with ground state I atoms) to possess an additional  $0.94$  eV, that is,  $1.60 \pm 0.04$  eV of translational energy. Conservation of energy dictates that the translational energy of the fastest H atoms formed is equal to the difference between the photolysis photon energy and the HI bond dissociation energy. A photolysis energy of  $266$  nm corresponds to  $4.66$  eV, which yields a HI bond strength of  $3.06 \pm 0.04$  eV. This experimentally determined value is in excellent agreement with the published HI bond energy of  $3.05$  eV.<sup>20</sup>

Normally the speed of the fastest photofragments may be determined by measuring the width of the vertical intensity profile where the intensity cross-section intersects the baseline. However, in these experiments, the intersection of the  $266$ -nm photolysis signal with the baseline is obscured by fragments arising from residual dissociation of HI by the ionization laser. These fragments, whose total intensity is less than  $10\%$  of the peak intensity, possess more kinetic energy because of the higher frequency photolysis wavelength. In order to extract the speed of the fastest fragments following  $266$ -nm photolysis, the edges of the  $266$ -nm distribution were linearly extrapolated to the baseline as indicated in Fig. 3.

As a further check of the quantitative nature of ion imaging, the speed of the fastest fragments arising from  $205$ -nm HI photolysis can also be used to determine the bond dissociation energy of HI. From Fig. 3 we calculate that the fastest H atoms from  $205$  nm photolysis moving perpendicular (vertical) to the detector axis possess  $2.05 \pm 0.04$  eV of translational energy. A photolysis energy of  $205$  nm corresponds to  $6.04$  eV, which, having taken into account the  $0.94$  eV  $I/I^*$  energy difference, yields a HI bond dissociation energy of  $3.05 \pm 0.04$  eV.

In order to make further quantitative assessments about the competing HI dissociation channels from this ion image, the 3-D velocity distribution is reconstructed from the image shown in Fig. 3. The algorithm used to perform a reconstruction is described in detail by Strickland and Chandler,<sup>32</sup> as was discussed briefly in the preceeding section of this chapter. Figure 4 shows the result of reconstructing the data image of Fig.3. The full 3-D distribution can be visualized by rotating Fig. 4 about its vertical axis.

The reconstructed 3-D velocity distribution shown in Fig. 4 clearly resolves the slower cosine-squared fragment velocity distribution from the higher-energy sine-squared distribution. The resolution of these competing dissociation channels allows for a determination of the amount of product in each channel, that is, a determination of the product branching ratio. This ratio has been traditionally expressed in the literature as the percentage of excited state iodine production ( $\%I^*$ ).<sup>8-10,19</sup> In order to extract the product branching ratio for  $266$ -nm HI photolysis from a reconstructed ion image, the photofragment radial

intensity distribution within a thin band centered around the radius of maximum intensity is plotted for each of the dissociation channels. A linear least-squares fit is then applied to each intensity distribution in

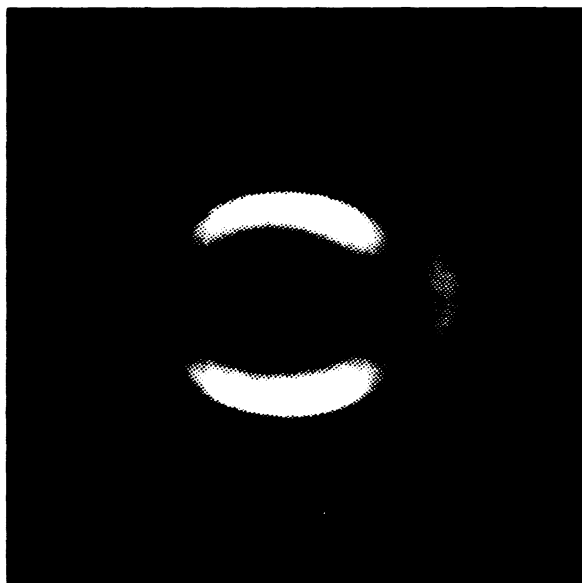


**Figure 2**

Ion image of the H-atom fragment distribution following 266-nm photolysis of HI. This two-dimensional projection of the three-dimensional velocity distribution clearly shows the competing cosine-squared (upper and lower lobes) and sine-squared (side lobes) fragment distributions corresponding to the production of  $I(^2P_{3/2})$  and  $I^*(^2P_{1/2})$ , respectively.

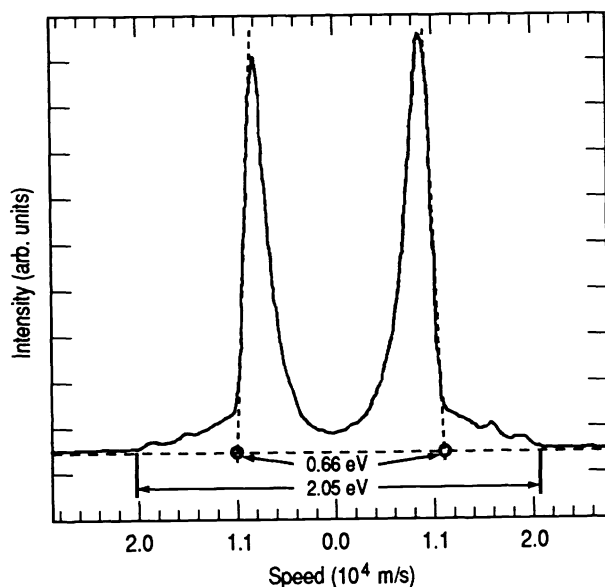


**Figure 3**

Intensity profile of Fig. 2 taken as a thin vertical slice down the center of the image. The speed of the fastest H atoms arising from the parallel dissociation channel following 266-nm photolysis is measured by extrapolation to the baseline as shown. Ion intensity at higher velocities arises from dissociation of residual HI by the 205-nm ionization laser. See text for details.

the form  $I(\theta) = A\cos^2\theta$  for the parallel dissociation channel, and  $I(\theta) = B\sin^2\theta$  for the perpendicular dissociation channel. Fig. 5 shows a representative fit to both the parallel and perpendicular dissociation channels. Both fits shown are taken from the same data set (ion image). The “best fit” parameters A and B for a given data set provide a measure of the amount of signal in each dissociation channel. However, a number of geometric factors need to be considered before a product branching ratio can be determined.

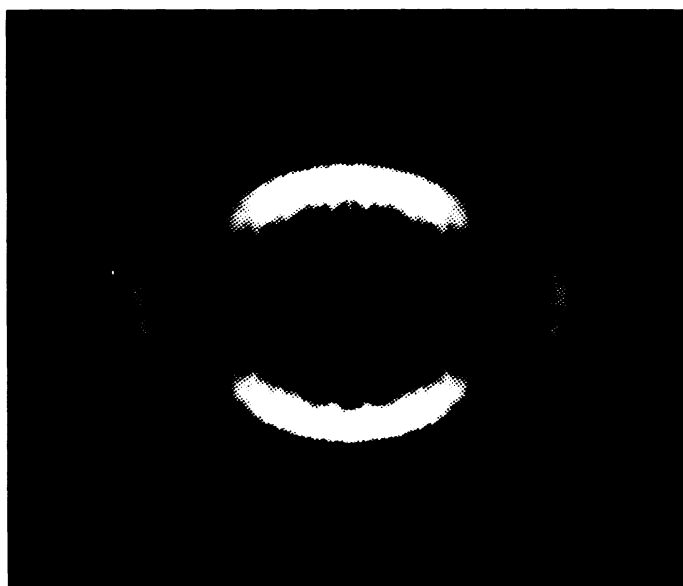


**Figure 4**

Thin slice of the reconstructed three-dimensional velocity distribution of H-atom photofragments following 266 nm HI photolysis.

Fragments from the perpendicular dissociation channel can be thought of as forming a sphere whose radius is 1.54 times larger than the sphere formed by the slower moving fragments. This value of 1.54 is calculated from the relative speeds of the fastest fragments from each dissociation channel as determined earlier. As the surface area of a sphere is proportional to the square of its radius, the best fit parameter B needs to be multiplied by  $(1.54)^2$ , or 2.39, to properly account for this geometric effect. It must be kept in mind that the perpendicular dissociation channel must be weighted by a further factor of two as compared to the parallel dissociation channel. This arises because for a parallel dissociation,  $\beta=2$ , twice the amplitude is in the angular distribution as for a perpendicular dissociation,  $\beta=1$ . A clear way to illustrate this point is to evaluate the intensity distributions for each of the limiting cases of parallel and perpendicular dissociation. This leads to angular distributions of the form:

$$I_{\text{parallel}}(\theta) = \frac{3}{4}\pi(\cos^2 \theta) \quad (1)$$

and

$$I_{\text{perpendicular}}(\theta) = \frac{3}{8}\pi(\sin^2 \theta) \quad (2)$$

The factor of two is clearly observed when comparing these two equations. Thus, the product branching ratio for HI dissociation may now be expressed in the form:



$$\frac{I^*}{I + I^*} = \frac{A}{A + (2 \times 2.39 \times B)} \quad (3)$$

The photodissociation product branching ratio is determined for four separate data sets (one of which constitutes the image shown in Fig. 2 and reconstructed in Fig 4 and the averaged result is %I\* = 38.4 +/- 2.3 in excellent agreement with each of the previously published results.

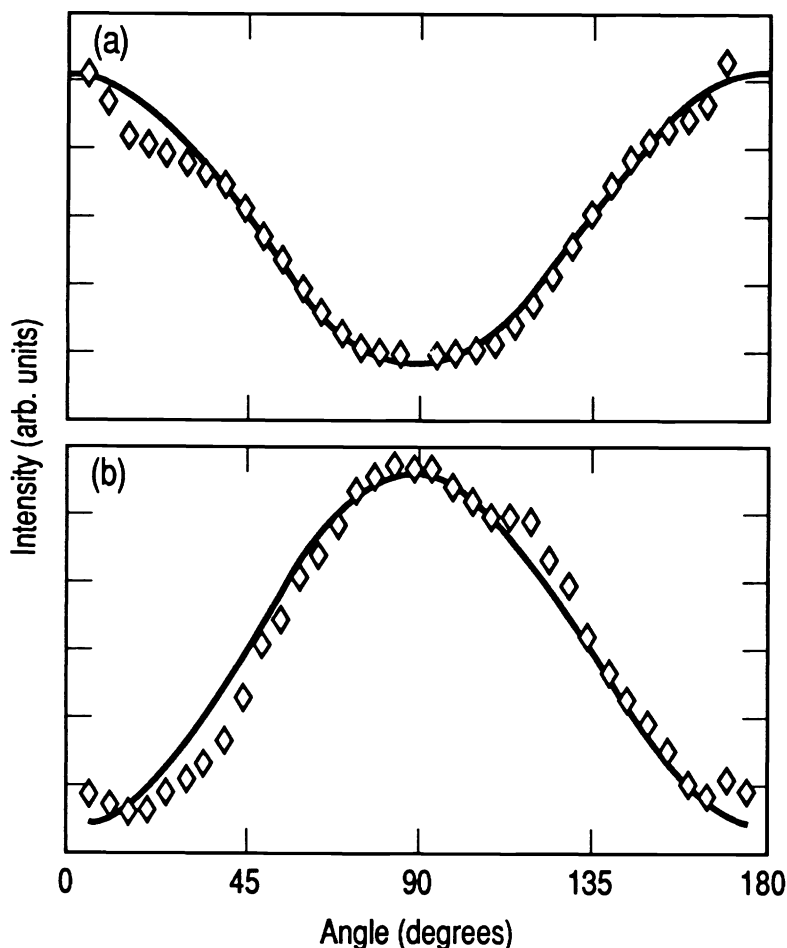


**Figure 5**

Representative fit of the HI photofragment radial intensity distributions. The solid lines represent a linear least-squares fit to the data points shown as open diamonds. (a) Fit of the form  $I(\theta) = A \cos^2\theta$  to the parallel dissociation channel. (b) Fit of the form  $I(\theta) = B \sin^2\theta$  to the perpendicular dissociation channel. The ratio of A to B is used to determine the photodissociation product branching ratio.

### 3. Bimolecular Reactions: $\text{H} + \text{D}_2 \rightarrow \text{HD} + \text{D}$

Ideally, one would like to measure the the velocity distribution, both speed and angular, of the reaction products the differential cross-section (DCS) measurement. This can only be done if the velocities of the reagents are well defined. Historically differential cross section measurements have been made possible only through crossed-beam time-of-flight experiments.<sup>34</sup> A typical experiment involves time-of-flight analysis of the products emitted at some angle with respect to a laboratory fixed direction (often this direction is chosen to be the direction of the reactant-atom beam). The detector position can be rotated,

allowing data to be collected at several angles. At each angle, only a small portion (typically  $10^{-4}$ ) of the products is detected, which results in long hours of signal averaging. Subsequently, normalization of the data to a fixed angle, and transformation of the data from the laboratory frame to the center of mass frame is necessary to obtain the DCS. In spite of the experimental challenges, state-resolved differential cross section measurements for  $D + H_2$  have been reported by Buntin *et al.*<sup>35</sup> for a few angles at collision energies of 0.8 eV and 1.20 eV, and by Continetti *et al.*<sup>36</sup> for a wide distribution of angles, at collision energies of 0.53 eV and 1.01 eV. In both experiments time-of-flight analysis of the HD product was sufficient to resolve individual vibrational, but not individual HD rotational states. In an alternative approach, Schnieder *et al.*<sup>37</sup> have used Rydberg atom time-of-flight translational spectroscopy to measure the vibrationally resolved differential cross section for the  $H + D_2$  reaction at collision energies of 0.54 eV and 1.29 eV. More recently, by reducing the energy spread in their  $D_2$  beam, Schnieder and Welge<sup>38</sup> have reported the first rotationally resolved differential cross section measurement for this fundamental reaction.

In order to study bimolecular reactions we have modified the apparatus to place a second molecular beam parallel to the one in which the HI photolysis was performed. The H atoms formed from the 226-nm photolysis of the HI collide with this second molecular beam of neat  $D_2$  and react to form  $HD + D$ . The product D atoms are ionized (1+1 REMPI) at the point of production by using 121.6-nm light, formed by frequency tripling 364.8 nm light in a Kr/Ar gas mixture. The D atom ions are allowed to travel down the time-of-flight tube and impact upon the position sensitive detector. In this manner a two-dimensional projection of the D atom product's Newton spheres is recorded. We label this technique Reaction Product Imaging (RPI). This is schematically shown in Fig. 6.

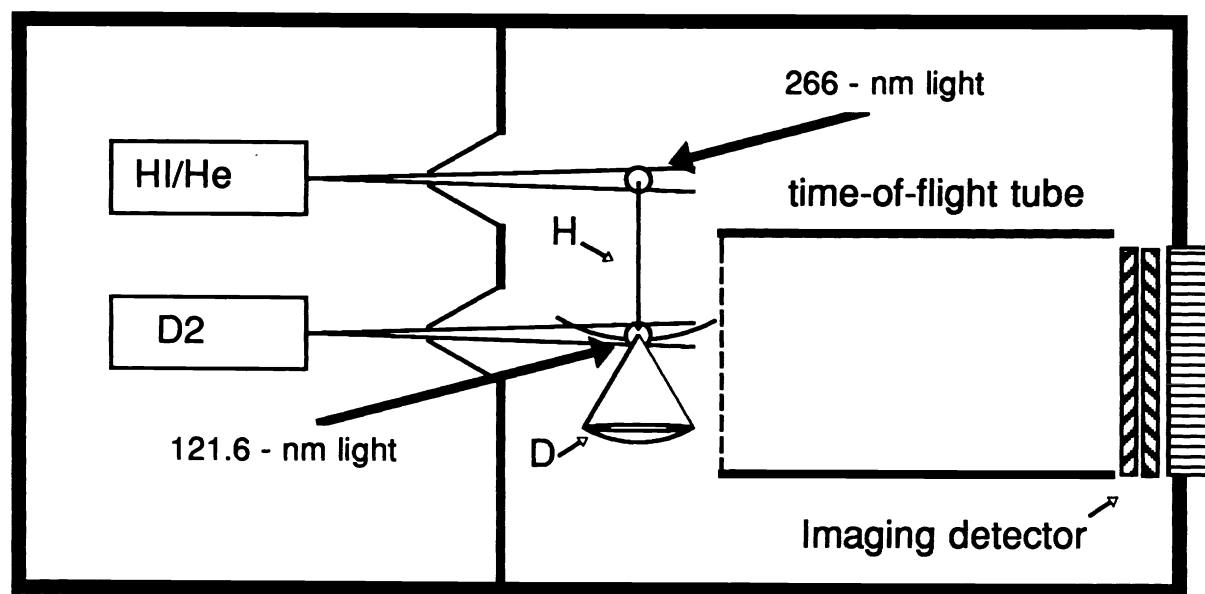


**Figure 6**

Schematic representation of the apparatus used to study bimolecular reactions using the imaging techniques.

In Fig. 7 is displayed the images of product D atoms obtained with this technique. In spite of the fact that we are unable to resolve individual quantum states of the HD product in the images of the D atoms, qualitative information pertaining to the reaction can be extracted from the images. On a qualitative level, inspection of Fig. 7 (a) ( $E_{CM}=0.54$  eV) reveals that the D atoms are strongly peaked along the beam direction of the H atoms and that their distribution is relatively narrow (there is not much intensity at velocities that would correspond to HD( $v=1$ ) being formed). This observation supports the theoretical predictions<sup>39-43</sup> that at low collision energies, HD will be formed predominantly in  $v=0$  and in low rotational states, and product D-atoms will be forward scattered with respect to the direction of the H-atom beam velocity.

Inspection of the reaction product image of Fig. 7 (b) ( $E_{CM}=1.29$  eV) reveals similar information. With the visual aid offered by the overlaid *Newton Circles*, for selected HD quantum states ( $v=0, J=0$ ), ( $v=1, J=0$ ), ( $v=2, J=0$ ), it is apparent that at wider scattering angles, formation of internally excited HD is the dominant channel of the reaction. Although very wide angle scattering is observed, no evidence appears of direct D-atom backscattering, (D atoms moving against the direction of the incoming H atoms), which would imply the formation of a long-lived complex near the transition state.

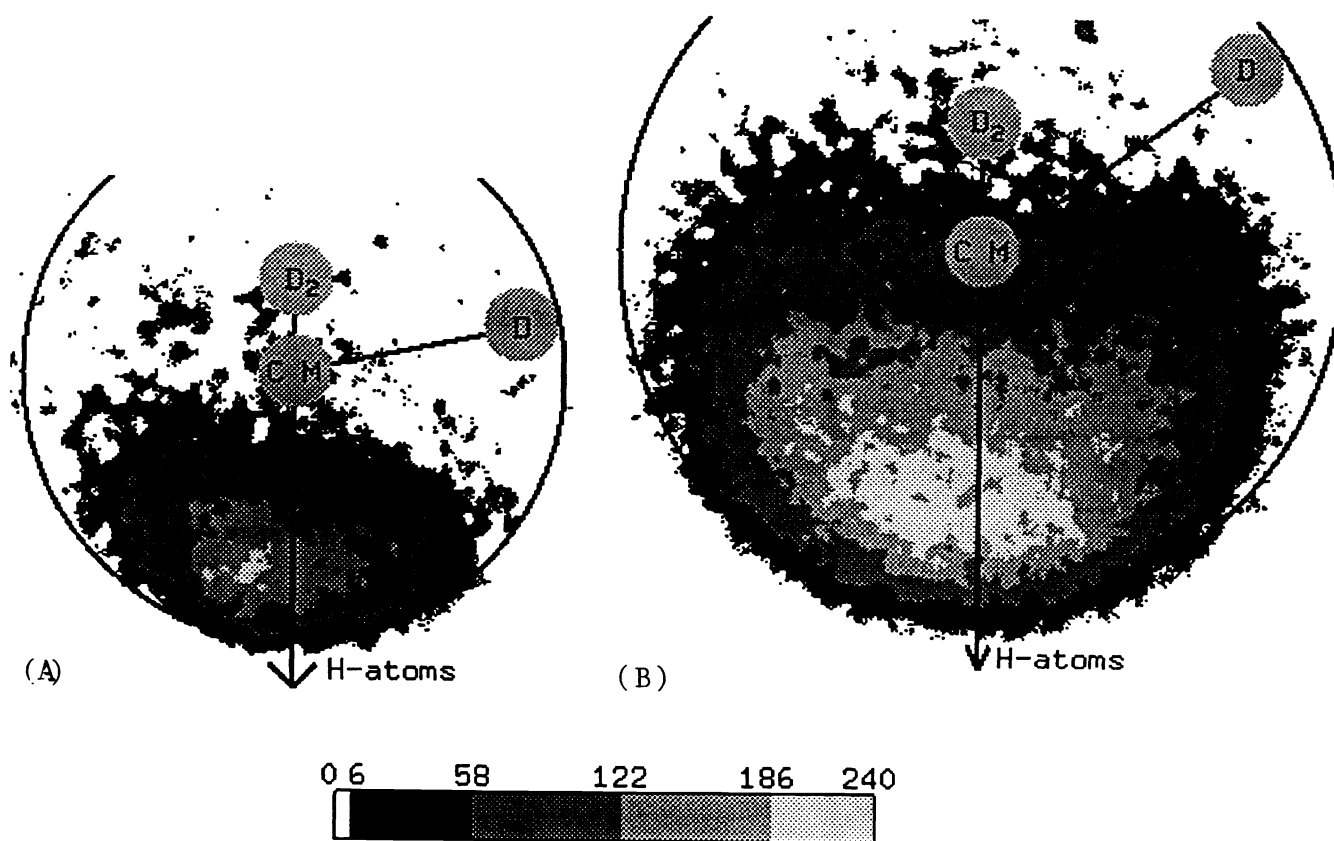


**Figure 7**

Images of the product D atoms produced from the reaction  $H + D_2 \rightarrow HD + D$  at nominal center-of-mass collision energies of 0.54 eV and 11.29 eV. The open circles represent the calculated position of scattered D atoms corresponding to HD ( $V=0, J=0$ ). the direction of the H atom beam is indicated by the arrow and the position of the  $D_2$  beam and the center-of-mass of the reaction are indicated by the solid circles labeled  $D_2$  and CM, respectively.

## 4. Conclusion

We have applied the photofragment ion imaging technique to the investigation of the 266-nm photodissociation dynamics of hydrogen iodide. This study has demonstrated the essential concepts behind the ion imaging technique and has shown that this method is highly quantitative in determining photofragment recoil velocity distributions, product branching ratios and bond dissociation energies.

We have developed a new ion imaging technique to study bimolecular reactive scattering, which we believe will be a very powerful method for studying reaction dynamics. There are several advantages offered by Reaction Product Imaging over traditional methods: (1) The  $4\pi$  particle collection efficiency leads to count rates capable of producing complete product angular distributions for the reaction within a few hours; (2) the technique samples the entire product angular distribution simultaneously; (3) a single quantum state of the product, in this case ground state D atoms, can be selected by utilizing REMPI.

## 5. Acknowledgments

We thank Mark Jaska for his expert technical assistance. MAB and RNZ thank the National Science Foundation (under NSF CHE 90-7939). This work was supported by the Department of Energy, Office of Basic Energy Sciences, Division of Chemical Sciences.

## 6. References

1. D. W. Chandler and P. L. Houston, *J. Chem. Phys.* **87**, 1445 (1987).
2. J. W. Thoman, Jr., D. W. Chandler, D. H. Parker and M. H. M. Janssen, *Laser Chem.* **9**, 27 (1988).
3. D. H. Parker, Z. W. Wang, M. H. M. Janssen and D. W. Chandler, *J. Chem. Phys.* **90**, 60 (1989).
4. D. W. Chandler, J. W. Thoman, Jr., M. H. M. Janssen and D. H. Parker, *Chem. Phys. Lett.* **156**, 151 (1989).
5. D. W. Chandler, M. H. M. Janssen, S. Stolte, R. N. Strickland, J. W. Thoman, Jr., and D. H. Parker, *J. Phys. Chem.* **94**, 4839 (1990).
6. H. Joswig, M. A. O'Halloran, R. N. Zare and M. S. Child, *Faraday Discuss. Chem. Soc.* **82**, 79 (1986); M. A. O'Halloran, H. Joswig and R. N. Zare, *J. Chem. Phys.* **87**, 303 (1987); E. Hasselbrink, J. R. Waldeck and R. N. Zare, *Chem. Phys.* **126**, 191 (1988); J. F. Black, J. R. Waldeck and R. N. Zare, *J. Chem. Phys.* **92**, 3519 (1990).
7. Z. Xu, B. Koplitz and C. Wittig, *J. Phys. Chem.* **92**, 5518 (1988); Z. Xu, B. Koplitz and C. Wittig, *J. Chem. Phys.* **90**, 2692 (1989).
8. R. Schmiedl, H. Dugan, W. Meier and K. H. Welge, *Z. Phys. A* **304**, 137 (1982).
9. R. D. Clear, S. J. Riley and K. R. Wilson, *J. Chem. Phys.* **63**, 1340 (1975).
10. G. N. A. Van Veen, K. A. Mohamed, T. Baller and A. E. De Vries, *Chem. Phys.* **80**, 113 (1983).
11. C. F. Goodeve and A. W. C. Taylor, *Proc. Roy. Soc. A* **152**, 221 (1935); *ibid* **A154**, 181 (1936) and references therein.
12. R. A. Ogg, Jr. and R. R. Williams, Jr., *J. Chem. Phys.* **13**, 586 (1945); R. R. Williams, Jr. and R. A. Ogg, Jr., *ibid* **15**, 691 (1947); R. R. Williams, Jr. and R. A. Ogg, Jr., *ibid* **15**, 696 (1947).
13. R. M. Martin and J. E. Willard, *J. Chem. Phys.* **40**, 2999 (1964).
14. B. J. Huebert and R. M. Martin, *J. Phys. Chem.* **72**, 3046 (1968); L. E. Compton and R. M. Martin, *ibid* **73**, 3474 (1969).
15. G. A. Oldershaw, D. A. Porter and A. Smith, *J. Chem. Soc. Faraday I* **68**, 2218 (1972).
16. R. J. Donovan and D. Husain, *Trans. Faraday Soc.* **62**, 1050 (1966); D. Husain and R. J. Donovan, *Adv. Photochem.* **8**, 1 (1971).

17. P. Brewer, P. Das, G. Ondrey and R. Bersohn, *J. Chem. Phys.* **79**, 720 (1983).
18. R. S. Mulliken, *Phys. Rev.* **51**, 310 (1937).
19. I. Levy and M. Shapiro, *J. Chem. Phys.* **89**, 2900 (1988).
20. H. Okabe, *Photochemistry of Small Molecules*, (Wiley, New York, 1978).
21. A parallel-type electronic transition within a diatomic molecule is one in which the transition electric-dipole moment lies along the molecular internuclear axis. Conversely, a perpendicular-type electronic transition occurs when the transition electric-dipole moment lies perpendicular to the internuclear axis.
22. R.D. Levine and R.B. Bernstein, *Molecular Reaction Dynamics and Chemical Reactivity* (Oxford University Press, 1987).
23. M. A. Buntine, D. P. Baldwin, R. N. Zare and D. W. Chandler, *J. Chem. Phys.* **94**, 4672 (1991); M. A. Buntine, D. P. Baldwin, R. N. Zare and D. W. Chandler, submitted to *J. Chem. Phys.* (1992).
24. W.M. Huo, K.-D. Rinnen and R.N. Zare, manuscript in preparation; K.-D. Rinnen, M.A. Buntine, D.A.V. Klinier, R.N. Zare and W.M. Huo, manuscript in preparation.
25. J.D. McDonald and D.R. Herschbach, *J. Chem. Phys.* **62**, 4740 (1975).
26. W. Bauer, L.Y. Rusin and J.P. Toennies, *J. Chem. Phys.* **68**, 4490 (1978); W.H. Beck, R. Götting, J.P. Toennies and K. Winkelmann, *J. Chem. Phys.* **72**, 2896 (1980).
27. P.M. Aker, G.J. Germann and J.J. Valentini, *J. Chem. Phys.* **90**, 4795 (1989); P.M. Aker, G.J. Germann, K.D. Tabor and J.J. Valentini, *J. Chem. Phys.* **90**, 4809 (1989).
28. D.A.V. Klinier, K.-D. Rinnen and R.N. Zare, *J. Chem. Phys.* **90**, 4625 (1989); K.-D. Rinnen, D.A.V. Klinier, M.A. Buntine and R.N. Zare, *Chem. Phys. Lett.*, **169**, 365 (1990).
29. D.A.V. Klinier, K.-D. Rinnen, M.A. Buntine, D.E. Adelman and R.N. Zare manuscript in preparation.
30. D. P. Baldwin, M. A. Buntine and D. W. Chandler, *J. Chem. Phys.* **93**, 6578 (1990).
31. R. N. Bracewell, *The Fourier Transform and its Applications* (McGraw-Hill, New York, 1986).
32. R. N. Strickland and D. W. Chandler, *App. Optics* **30**, 1811 (1991).
33. C. E. Moore, *Atomic Energy Levels Volume III*, NSRDS-NBS (1971).
34. R. Goetting, H.R. Mayne, and J.P. Toennies, *J. Chem. Phys.* **80**, 2230 (1984); **85**, 6396 (1986).
35. S.A. Buntin, C.F. Giese, and W.R. Gentry, *J. Chem. Phys.* **87**, 1443 (1987); *Chem. Phys. Lett.* **168**, 513 (1990).
36. R.E. Continetti, B.A. Balko, and Y.T. Lee, *J. Chem. Phys.* **93**, 5719 (1990).
37. L. Schnieder, K. Seekamp-Rahn, F. Liedeker, H. Steuwe, and K.H. Welge, *Faraday Discuss. Chem. Soc.* **91**, 259 (1991).
38. L. Schnieder and K.H. Welge, *XIVth International Symposium on Molecular Beams*, Abstracts of Invited Talks and Contributed Papers Asilomar, USA, June 7-12, 1992, p. 27.
39. D. L. Phillips, H. B. Levene and J. J. Valentini, *J. Chem. Phys.* **90**, 1600 (1989); J. C. Nieh and J. J. Valentini, *ibid* **92**, 1083 (1990).
40. N. Blais and D. G. Truhlar, *Chem Phys. Lett.* **162**, 503 (1989); N. C. Blais, M. Zhao, M. Mladenovic, D. G. Truhlar, *J. Phys. Chem.* **94**, 6696 (1990).
41. F. J. Aoiz, V. J. Herrero, O. Puentedura and V. Saez Rabanos, *Chem. Phys. Lett.* **169**, 243 (1990); F. J. Aoiz, V. J. Herrero and V. Saez Rabanos, *J. Chem. Phys.* **97**, 7423 (1992).
42. D. E. Manolopoulos and R. E. Wyatt, *Chem Phys. Lett.* **159**, 123 (1989); M. D'Mello, D. E. Manolopoulos and R. E. Wyatt, *J. Chem. Phys.* **94**, 5985 (1991).
43. J. Z. H. Zhang and W. H. Miller, *Chem Phys. Lett.* **153**, 465 (1988); *ibid* **159**, 130 (1989); *J. Chem. Phys.* **91**, 1528 (1989).